Ocean Engineering 339 (2025) 122062

Contents lists available at ScienceDirect

Ocean Engineering

journal homepage: www.elsevier.com/locate/oceaneng

Research paper

Performance characteristics of the Archimedes screw hydrokinetic turbine

Temitope E. Phillips [a,*], David H. Wood [b]

[a] University of Calgary, Canada
[b] Emeritus Professor of Renewable Energy, University of Calgary, Canada

ARTICLE INFO

Keywords:
Torque ripple
Archimedes screw turbine
Performance characteristics
River and tidal energy conversion
Power output
Torque generation mechanism
Energy conversion mechanism

ABSTRACT

The Archimedes Screw hydrokinetic turbine (AST) is garnering considerable interest because of its potential applicability in harvesting river and tidal energy. The turbine is well suited to bi-directional flows, low-velocity flows, and shallow watercourses. Because the AST is a reasonably new hydro-technology, very little literature is available on its design and performance optimization. This study experimentally investigates the torque and power generation of the AST. Laboratory scale turbine models with one, two, and three flights (blades) were tested in a water tunnel to measure torque and angular velocity at different flow velocities and varying inclination angles (β) of the turbine. A maximum coefficient of performance (C_P) of 0.41 was obtained at a tip speed ratio (λ) of 0.52 at a flow velocity (U_∞) of 0.45 m/s and $\beta = 30°$ for a turbine with two flights. In the case of the 3-flight turbine, the highest value of C_P was also obtained at 30° (0.40 at $\lambda = 0.53$). For the 1-flight turbine, a maximum C_P of 0.23 was obtained at a β of 28° and λ of 0.30. The results also showed a time-varying fluctuation in the torque, which reduced in magnitude with an increase in number of flights. The ripple was found to occur once-per-revolution and not once-per-flight, irrespective of the number of flights.

1. Introduction

The Archimedes screw turbine (AST), shown in Fig. 1a, is a hydrokinetic turbine that can be used in small hydropower systems, which are fast becoming a reliable means of generating power in remote and off-grid locations where reasonable hydropower resources are readily available. It is different from the more popular Archimedes screw generator (ASG) shown in Fig. 1b by the absence of the casing enclosing the blades so that it converts the kinetic energy of the water flow rather than the low head of the ASG. The differences between the AST and ASG are discussed in more detail in Section 2.

There is an abundance of flow-of-the-river and tidal resources that the AST can exploit. The turbine is suited to bi-directional flow, making it an excellent candidate for harvesting tidal energy. It is also well suited for very low current speeds (Shahsavarifard et al., 2015; Zhang et al., 2023) and other low-flow-rate conditions where most other turbine types cannot operate optimally (Williamson et al., 2011). This could be important for water resources with significant flow variation throughout the year.

The chief advantage of the AST is its simplicity and ruggedness making it cheap to manufacture and resilient to water-bourne debris. It is also a low-speed turbine whose maximum torque occurs when the turbine is stationary so that it starts easily. Its low-speed operation also means that the likelihood of the occurrence of cavitation during its operation is low. Like a vertical-axis turbine, the AST is easily configured so the generator is above water as shown in Fig. 1a.

The AST is of potential economic importance because of its simple design, sturdy construction, and its prospects of a long lifespan. Due to its simple design, it can be easily manufactured in developing countries and remote locations using locally available materials and technologies at low costs. Its more popular and better-known counterparts like the Kaplan and Francis turbines have more complex designs and are expensive to manufacture and are hence very likely to be out of reach within these target communities. In addition, the AST has the capability to operate at flow speeds that are relatively low compared to vertical and horizontal axis hydrokinetic turbines.

The AST can be instrumental in filling the need for clean, renewable, sustainable, and affordable energy. Providing an efficient turbine design could be of great economic and environmental importance. The literature review in Section 2 will show that very little is currently known about the hydrodynamics of the AST. This study aims to address some of the gaps in the literature regarding the AST to better understand its operation by undertaking experiments to determine its performance characteristics.

The remainder of this paper has the following organisation. The limited literature on the AST is reviewed in the next Section. The experimental setup and measurements are described in Section 3 and the results in Section 4. The final section contains the conclusions.

* Corresponding author.
E-mail address: temitope.phillips@ucalgary.ca (T.E. Phillips).

https://doi.org/10.1016/j.oceaneng.2025.122062
Received 18 January 2025; Received in revised form 24 June 2025; Accepted 24 June 2025
Available online 3 July 2025

(a) AST

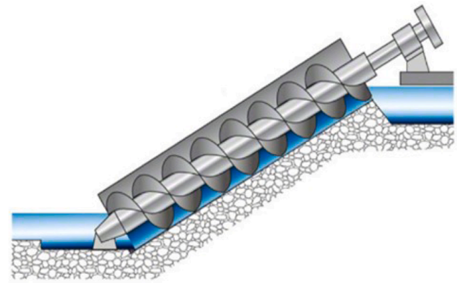

(b) ASG

Fig. 1. Geometric differences between the AST (left) and ASG (right).

Table 1
List of Symbols.

Symbol	Quantity	Unit
β	Inclination angle	Degrees °
δ	Diameter ratio	
ϵ	Blockage ratio	
λ	Tip speed ratio	
ω	Angular velocity	rad/s
Λ	Turbine pitch	m
Λ_r	Pitch ratio	
ρ	Density	kg/m^3
τ	Torque	Nm
A	Water channel cross sectional area	m^2
A_t	Turbine swept area	m^2
C_P	Power coefficient	
C_τ	Torque coefficient	
D, d	Turbine outside and inside diameters	m
f_n	Low-pass frequency	Hz
L	Turbine length	m
L_r	Length ratio	
N	Number of flights	
R	Turbine radius	m
P	Power	W
P_t	Turbine power	W
U_∞	Freestream velocity	m/s

2. Review of available literature

The Archimedes screw originated in the middle of the second century BC as a positive displacement pump (Alton and Howell, 2003; Nagel, 1968; Rorres, 2000; Thakur et al., 2024). Over the years, the screw found application in myriad applications: water pumps, fish ladders, sewage pumps, grain pumps, and heart valve replacement devices. It was in the latter part of the twentieth century that the screw started to be researched as a form of hydro turbine.

A large portion of available literature and research data focuses on the operation of the Archimedes screw turbine as a function of the available head rather than on the kinetic energy of moving water. When harnessing the potential energy of water due to a head difference, the turbine will be referred to as an Archimedes Screw Generator (ASG). The ASG is essentially an Archimedes screw enclosed within a casing and operated at an angle to the horizontal (see Fig. 1b). Buckets are formed between the screw blades and the casing. These buckets trap water between the blades (Rorres, 2000; Lyons and Lubitz, 2013; Kozyn et al., 2015; Simmons and Lubitz, 2017; Shahverdi et al., 2021) and the head difference between buckets generates pressure on the screw causing it to rotate (Shimomura and Takano, 2013; Waters, 2015; Kozyn et al., 2015; Shahverdi et al., 2021).

The first Archimedes Screw hydro turbine was tested in 1995 at the Technical University in Prague, and the first operational ASG was installed on the river Eger in Aufhausen, Germany, in 1997 (Lashofer et al., 2012). In the early 2000s, it was introduced to the UK (Waters and Aggidis, 2015) and in September 2013, the first ASG was connected to the North American power grid in Ontario (Kozyn et al., 2015). There are presently about 400 installations of the ASG of varying sizes around the world, with the majority of these installations in Europe (Lashofer et al., 2012; Kozyn et al., 2015).

Even though the ASG operates at very low heads, it still requires at least a 1 m head difference between the blades upstream and downstream for its operation. This head difference usually results from its inclination, and no hydrostatic force is created in the absence of an inclination (Rorres, 2000). The maximum efficiency of the ASG is limited by a combination of geometry and mechanical losses (Waters, 2015; Müller and Senior, 2009; Rohmer et al., 2016).

The AST is effectively an ASG without a casing and, therefore, does not form buckets (Fig. 1). It can be partially or fully submerged in water and placed horizontally or at an angle (β) to the horizontal. Unlike the ASG which utilises a hydrostatic head, the AST uses kinetic energy to produce a pressure difference between the upstream and downstream sides of the blades. The pressure difference produces a torque about the axis of rotation of the turbine.

There is still very little research on the AST, either experimental or numerical. The only large-scale prototypes reported in the literature are the Delta unit and the Cat 3EC42 deployed by Jupiter Hydro (Shahsavarifard et al., 2015). The Cat 3EC42 prototype, which is Jupiter Hydro's latest prototype, consists of two 0.91 m diameter, 2.85 m long ASTs fixed to an equilateral triangular platform. Each turbine was connected to a 3-kW synchronous permanent magnet generator, with the generator upstream of the turbine. They were able to obtain a maximum power coefficient (C_P) of 0.5 for one of the turbines (see Figs. 2 and 3). The mechanical power was obtained by direct

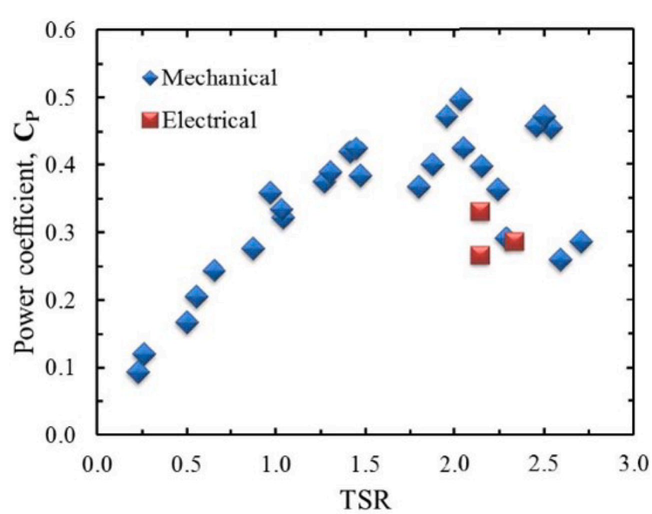

Fig. 2. Plot of C_P against λ (TSR) for the Energy CAT 3EC42. Reproduced from Shahsavarifard et al. (2015).

Table 2
Summary of Shahsavarifard et al. (2015)'s, Zhang et al. (2023)'s, and Zitti et al. (2020)'s results.

Ref.	D (m)	L (m)	Λ (m)	β	λ	C_P	Type
Shahsavarifard et al. (2015)	1.06	2.87	0.60	30°	2.04	0.500	Field Test
Zhang et al. (2023)	0.30	0.30	0.15	0°	1.20	0.350	CFD
Zitti et al. (2020)	0.10	0.32	0.16	10°	0.75, 0.1112	0.144, 0.07	CFD, Experiments
Zitti et al. (2020)	0.10	0.32	0.16	0°	0.75, 0.1117	0.238, 0.12	CFD, Experiments

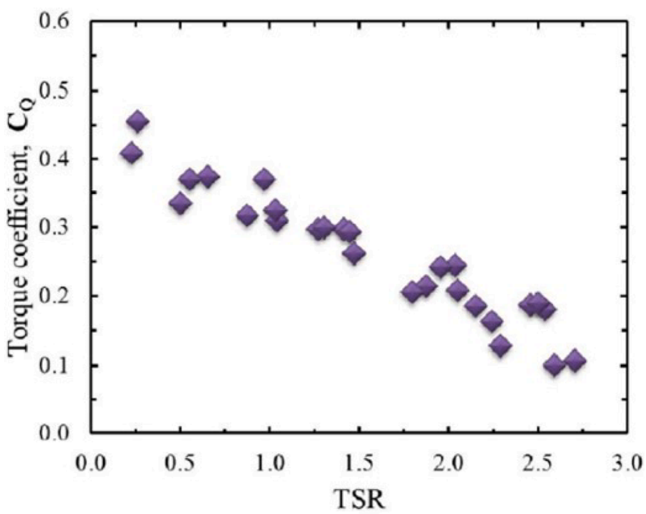

Fig. 3. Plot of C_τ against λ (TSR) for the Energy CAT 3EC42. Reproduced from Shahsavarifard et al. (2015).

measurement of the shaft torque and is therefore the energy extracted from the water. The electrical power is the output power from the generator and includes the generator efficiency. They also obtained maximum torque (τ) at tip speed ratio (λ) of 0.5, with torque coefficient (C_τ) decreasing as λ increased.

In terms of torque (τ), the power extracted from the water (P) can be expressed as:

$$P = \tau\omega \tag{1}$$

where ω is angular velocity. When the blades are stationary, $P = 0$. What is desired in any operation is for C_P to increase rapidly from zero as the speed increases. Differentiating both sides of Eq. (1) gives:

$$\frac{dP}{d\omega} = \omega\frac{d\tau}{d\omega} + \tau \tag{2}$$

Eq. (2) shows that when $\omega = 0$, τ is the rate of change of P with respect to ω, and that maximum τ always occurs below maximum power in terms of λ. The smaller the λ at which maximum P is obtained, the higher the starting torque will be. This analysis shows that because the AST achieves its best performance at low shaft speeds, it will have good self-starting capabilities. Zhang et al. (2023)'s work supports this analysis. They proposed an AST array for in situ power generation in deep-sea environments, and the results from their CFD simulations showed that the AST can start at speeds as low as 0.1 m/s and achieve average C_P values of up to 0.35 (see also Zhang et al., 2022).

In their investigations, Zhang et al. (2023) arranged three AST units in a triangular layout, with one turbine upstream of the other two. They chose this layout to maximise coupling effects between the turbines, optimise space utilisation for deep-sea deployment, and to facilitate the study of both co-rotating (all three turbines spinning in the same direction) and counter-rotating (upstream and downstream turbines spinning in opposite directions) setups. They modelled the opposing rotation for the counter-rotating configuration using CFD (ANSYS Fluent) by assigning opposite rotational directions (angular velocity vectors) to the downstream turbines compared to the upstream one. This allowed them to analyse the effect of opposite wake interactions, specifically how the meshing effect of the wake improves downstream performance and overall energy density. The co-rotating setup achieved a 6 % maximum C_P improvement over that of a single turbine operating in an open-flow field, and the counter-rotating setup achieved an 8 % improvement. This is because the counter-rotating setup reduces wake interference between the turbines and increases energy density by allowing tighter spacing. It also produces synergistic vortex structures that increase downstream turbine performance. It is important to note that the turbine models used in these investigations have a non-zero blade curvature, i.e. the blade is not mirror-symmetrical. One side of the blade is concave while the other side is convex. The present study used straight blades.

Zitti et al. (2020) conducted both experimental and computational studies on a small AST model and found that the performance coefficients obtained were in line with those for other types of hydrokinetic turbines. They recorded an average C_P of 0.07 from experiments and 0.15 from numerical simulations for their AST model, which had D = 0.1 m, Λ = 0.16 m, L = 0.32 m, N = 1, β = 10° and two turns. Their comparatively low values could be attributed to the lower value of β and the relatively smaller model size. Table 2 summarises the results of Shahsavarifard et al. (2015), Zhang et al. (2023), and Zitti et al. (2020).

A final advantage of the AST is that it can operate with either left-to-right flow or the reverse in Fig. 1. This would make it unnecessary to alter the turbine orientation in a tidal flow, for example, which would simplify installation. If the turbine flights are well below the water surface, the direction of flow should be immaterial, but if the turbine is located close to the water surface, which is likely for practical reasons, the free surface may influence the performance. This motivated us to test the AST with both flow directions.

3. Experimental methodology

3.1. Turbine geometry

The parameters that determine the geometry of the AST (Fig. 4) can be classified into external and internal parameters. The external parameters are those that are likely to be influenced by the site in which the

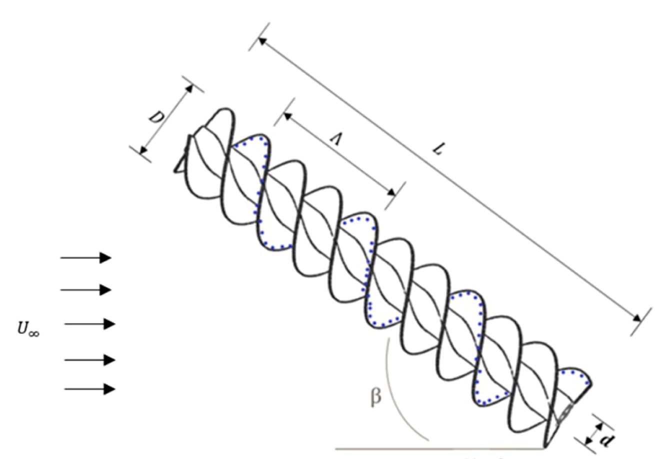

Fig. 4. Geometric configuration of the AST.

screw will be deployed, and they include the outside diameter (D) and the total length of the screw (L). The internal parameters are those that are required in addition to the external parameters to fully specify the screw's geometry and which can be modified to optimise the performance of the screw. They are the inside diameter (d), the pitch (Λ), and the number of flights (N).

1. External Parameters
   (a) Outside Diameter (D): This is the diameter of the coaxial circle whose circumference coincides with the crests of the blades.
   (b) Total Length of screw (L): This is the overall length of the turbine flights.
2. Internal Parameters
   (a) Inside Diameter (d): This is the diameter of the screw's inner cylindrical shaft around which the blades are wrapped.
   (b) Pitch (Λ): This is the distance between corresponding points on adjacent threads of the same flight, measured parallel to the axis of the screw.
   (c) Number of Flights (N): This is the number of blades/helices on the turbine and is equivalent to the number of blades in other turbine types.
3. Important Design Ratios
   (a) Diameter Ratio ($\delta = d/D$): If τ depends on the pressure difference across the turbine's blades (i.e. τ depends on pressure and $D - d$), then as d approaches D (reducing δ), τ would decrease and would approach zero when d is almost equal to D. In the same way, as d approaches zero, τ would also approach zero. This implies that there would be an optimal δ at which the maximum possible τ can be obtained.
   (b) Pitch Ratio ($\Lambda_r = \Lambda/D$): Literature on the ASG and ASP have shown that Λ_r has an important influence on the performance of these devices. This ratio could be of great importance to the AST as well.
   (c) Length Ratio ($L_r = L/D$): The length of the turbine is a direct function of the number of flights and the pitch. It is postulated that there could be an optimal maximum length that would produce maximum power output before the effects of weight and rotational inertia start to be dominant. There would also be a minimum length below which the pressure difference between the upstream and downstream sections of the turbine would be insignificant.

3.2. Experimental setup

To carry out tests on turbine models in the two flow directions in a unidirectional tunnel, the turbine models were inclined in two different configurations as shown in Fig. 5. In the first configuration, the turbine was inclined "against" the flow direction of the water and the instrumentation was upstream of the turbine as shown in Fig. 5a. In the second configuration, the turbine is inclined "into" the flow and the instrumentation was downstream of the turbine as shown in Fig. 5b. The turbine's performance would be expected to be the same for the two configurations when surface effects are negligible.

The water channel used is an Eidetics 1520 water tunnel with a test section that is 1.2 ft x 1.2 ft x 15 ft long (0.365 m x 0.365 m x 4.57 m long) and provides an adjustable free stream flow speed between 0.07 m/s and 0.45 m/s. It is a recirculating closed-circuit tunnel with a free water surface in the test section. The contraction upstream of the test section has an inlet/outlet area ratio of 6:1, which gives a uniform velocity distribution and turbulence level (the turbulence intensity is less than 1.0 % RMS) and avoids the likelihood of local flow separations. The turbine model shown in Fig. 5 has the following geometric properties:

1. $D = 100.2$ mm. This value was selected based on the dimensions of the water tunnel and the effects of blockage.
2. $\delta = 0.5$. Hence, $d = 50.1$ mm
3. $\Lambda_r = 1.4$. Hence, $\Lambda = 0.142$ m
4. $N = 3$ flights spaced at 120° to each other.
5. Number of turns (number of complete revolutions of the flights) = 3.5
6. $L = 3.5\Lambda = 0.497$ m

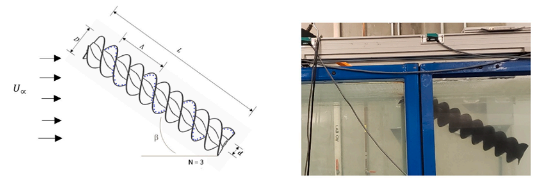

(a) First turbine configuration. Flow is from left to right.

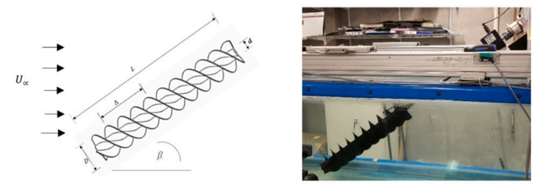

(b) Second turbine configuration. Flow is from left to right.

Fig. 5. Turbine orientation and experimental configurations.

3.3. Instrumentation

A Futek TQ513-062 rotary torque sensor was used to measure the torque exerted on the turbine as water flows over it. Thus, we measured the equivalent of the "mechanical power" in Fig. 2. A Warner Electric MPB2-1-24 magnetic particle brake was used to apply variable torque to the turbine shaft to accommodate changes in shaft rotational speed at different flow rates. A US Digital HB5M hollow bore optical encoder was used to measure the RPM of the turbine, and an ATI Gamma SI-32-2.5 force/torque sensor was used to measure forces. For data collection, the values of β and flow velocity (U_∞) were varied, while values of τ, and ω were recorded. Data was taken for turbines with one, two, and three flights in the two configurations.

The torque sensor measures the shaft torque which is the torque extracted from the water. A Futek IAA100 analog amplifier with voltage output amplified the signal before going into a data acquisition device (DAQ 6212). Using scripts written in Matlab, the torque data was obtained directly from the torque sensor. Data from the HB5M optical encoder were also processed through Matlab scripts, and the angular velocity was calculated from the RPM data. The power coefficient was obtained using Eq. (1):

$$C_P = \frac{P}{\frac{1}{2}\rho A_t U_\infty^3} = \frac{\tau\omega}{\frac{1}{2}\rho A_t U_\infty^3} \tag{3}$$

where ρ is the fluid density, and A_t is the turbine's swept area, which is defined as

$$A_t = LD\sin\beta \tag{4}$$

$$C_\tau = \frac{\tau}{\frac{1}{2}\rho A_t R U_\infty^2} = \frac{4\tau}{\rho L D^2 \sin\beta U_\infty^2} \tag{5}$$

Fig. 6 shows the instrumentation and how they are connected to the turbine in the experimental setup.

3.4. Error analysis

The uncertainties in the torque ($\Delta\tau$), angular velocity ($\Delta\omega$), tip speed ratio ($\Delta\lambda$), turbine power (ΔP_t), power coefficient (ΔC_P) and torque coefficient (ΔC_τ) were determined using the methods defined by

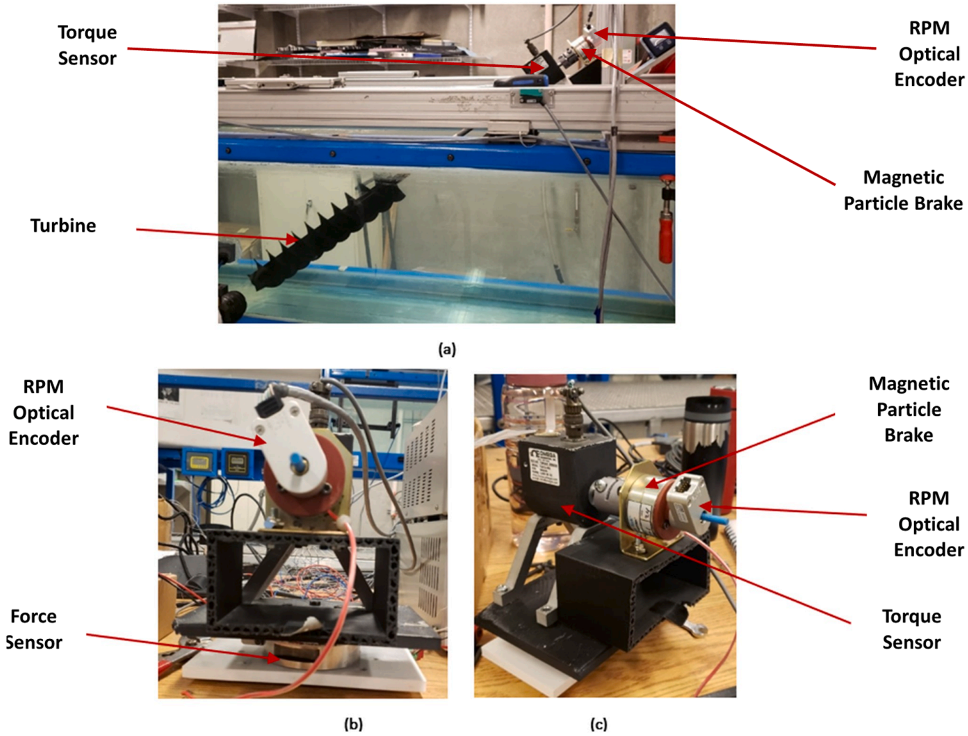

Fig. 6. Experimental setup with instrumentation (a) rig with turbine in the water tunnel with flow from left to right, (b) and (c) close-up of instrumentation.

Moffat (1982) and Taylor and Thompson (1998). The propagated errors in these quantities were estimated as follows:

$$\Delta\tau = \tau\sqrt{\left(\frac{\delta l}{l}\right)^2 + \left(\frac{\delta h}{h}\right)^2 + \left(\frac{\delta z}{Z}\right)^2} \tag{6}$$

where $\delta l/l$, $\delta h/h$, and $\delta z/z$ are the linearity, hysteresis, and zero error uncertainties in the torque sensor respectively, as provided by the manufacturer (Omega Engineering, 2000).

$$\Delta\omega = \omega\sqrt{\left(\frac{\delta v}{v}\right)^2 + \left(\frac{\delta T}{T}\right)^2 + \left(\frac{\delta\rho}{\rho}\right)^2} \tag{7}$$

where $\delta v/v$ and $\delta T/T$ are the uncertainties in the velocity uniformity and turbulent intensity level in the water tunnel respectively, as provided by the manufacturer (Rolling Hills Research Corporation, 2003), and $\delta\rho/\rho$ is the water density uncertainty, which is assumed to be 0.001 kg/m^3.

$$\Delta\lambda = \lambda\sqrt{\left(\frac{\Delta\omega}{\omega}\right)^2} \tag{8}$$

$$\Delta P_t = P_t\sqrt{\left(\frac{\Delta\omega}{\omega}\right)^2 + \left(\frac{\Delta\tau}{\tau}\right)^2} \tag{9}$$

$$\Delta C_P = C_P\sqrt{\left(\frac{\Delta P_t}{P_t}\right)^2} \tag{10}$$

$$\Delta C_\tau = C_\tau\sqrt{\left(\frac{\Delta\tau}{\tau}\right)^2} \tag{11}$$

These errors are typical and were fully analysed in Phillips (2024).

4. Experimental results

Table 3 shows the details of the experiments documented in this paper. For each case number, the first numerical value indicates the configuration (1 for the first configuration and 2 for the second configuration), and the second numerical value specifies the number of flights.

Table 3
Details of experimental cases.

Case	U_∞ (m/s)	β	Configuration	N
E1-3	0.45	30°	First	3
E1-2	0.45	30°	First	2
E1-1	0.45	30°	First	1
E1-v3	various	various	First	3
E1-v2	various	various	First	2
E1-v1	various	various	First	1
E2-3	0.45	30°	Second	3
E2-2	0.45	30°	Second	2
E2-1	0.45	30°	Second	1
E2-v3	various	various	Second	3
E2-v2	various	various	Second	2
E2-v1	various	various	Second	1

As shown in Table 3, the variations in C_P and λ have been obtained by varying the values of U_∞ while keeping β constant for Cases E1-v3, E1-v2, E1-v1, E2-v3, E2-v2, and E2-v1. Variations in U_∞ were small, so significant Reynolds number effects were unlikely.

4.1. Torque and power results for the first configuration

Fig. 7 shows the plot of C_P against λ for a 3-flight turbine at different values of β in the first configuration (Case E1-v3). A maximum C_P value of 0.40 was obtained at $\lambda = 0.53$. This value is relatively high and is close to the Betz-Joukowsky limit.

Shahsavarifard et al. (2015) and Zhang et al. (2023, 2022) also recorded high maximum C_P values (0.5 and 0.35 respectively). It is, however, important to note that (Shahsavarifard et al., 2015) described a field test in which blockage effects were negligible. It is also necessary to note the important geometric difference between (Zhang et al., 2023)'s model and that used in this current work, and that is the non-zero blade curvature in their model.

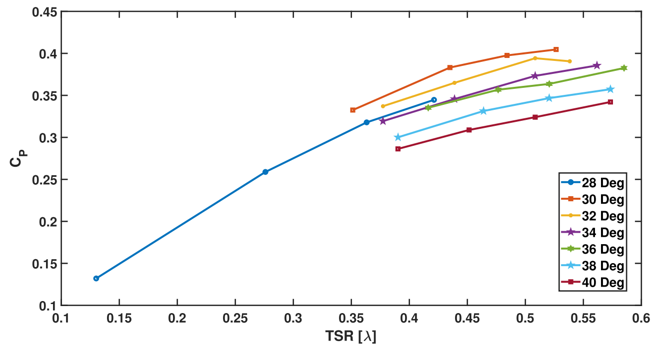

Fig. 7. C_P against λ for Case E1-v3.

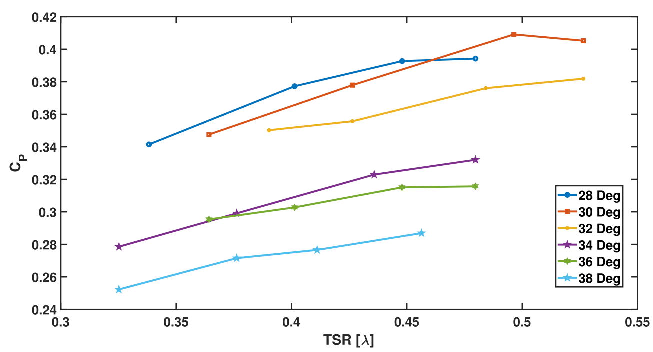

Fig. 8. C_P against λ for Case E1-v2.

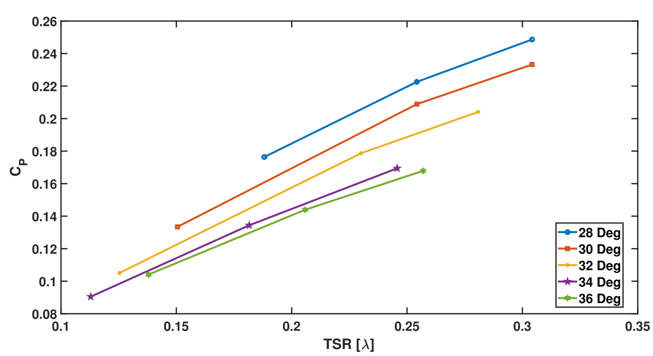

Fig. 9. C_P against λ for Case E1-v1.

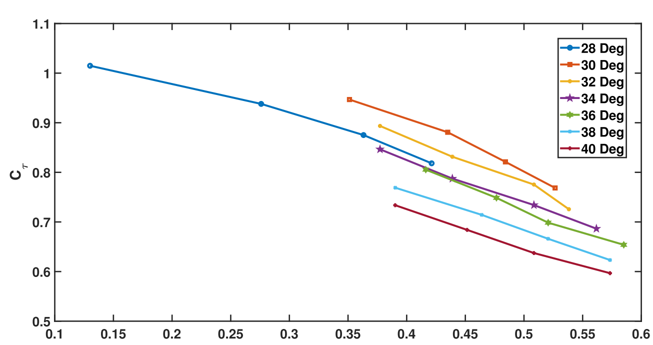

Fig. 10. C_τ against λ for E1-v3.

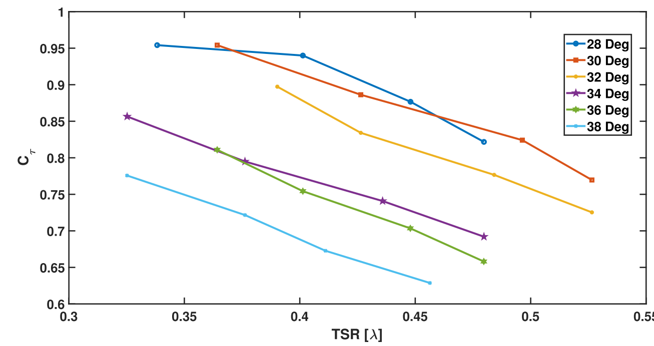

Fig. 11. C_τ against λ for Case E1-v2.

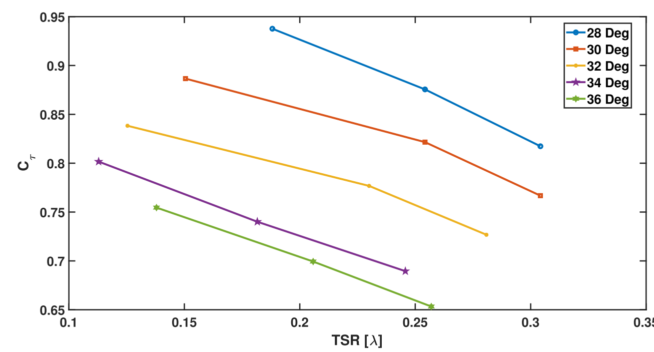

Fig. 12. C_τ against λ for Case E1-v1.

There are two possible explanations for the high C_P values obtained in the current work. The first is the effects of blockage as the blockage ratio $\epsilon = A_t/A = 0.187$. Values above 0.1 have been shown to affect turbine performance appreciably (Eltayesh et al., 2019; Jeong et al., 2018; Kinsey and Dumas, 2017; Kolekar and Banerjee, 2015; Ross and Polagye, 2020) principally by increasing C_P and C_τ. The other possible explanation for the high C_P values is the fact that the model of the vanishingly thin actuator disc at right angles to the flow, upon which the Betz-Joukowsky limit is based, might not be an accurate representation of the AST. The turbine's streamwise extent suggests using the alternative of a sequence of actuator discs in deriving performance maxima.

Shahsavarifard et al. (2015) also reported maximum C_P at $\beta = 30°$. However, the values of λ at which maximum C_P and C_τ were obtained in these experiments are smaller by about 74 % compared to Shahsavarifard et al.'s values (Figs. 2 and 3). This could result from the differences in the sizes between their full-scale model and the small-scale models used in these experiments. It could also depend on the geometric differences between the two models (pitch, number of flights, and number of turns).

In the case of the 2-flight turbine (Case E1-v2), the highest value of C_P of 0.41 was also obtained at 30° and $\lambda = 0.49$ (Fig. 8). In the case of the 1-flight turbine (Case E1-v1), a maximum C_P of 0.24 was obtained at $\lambda = 0.30$ at $\beta = 28°$ as shown in Fig. 9. It can also be observed that the tip speed ratio increases for maximum C_P with an increase in the number of flights, as observed by Consul et al. (2009) for crossflow turbines.

Figs. 10–12 show the plots of C_τ against λ for Cases E1-v3, E1-v2, and E1-v1 respectively. These figures show that C_τ is maximised at $\lambda = 0$, so the AST will likely start quickly as the water speed increases. In Fig. 13, C_P and C_τ have been plotted together for Case E1-v3. Error bars have been included in these plots.

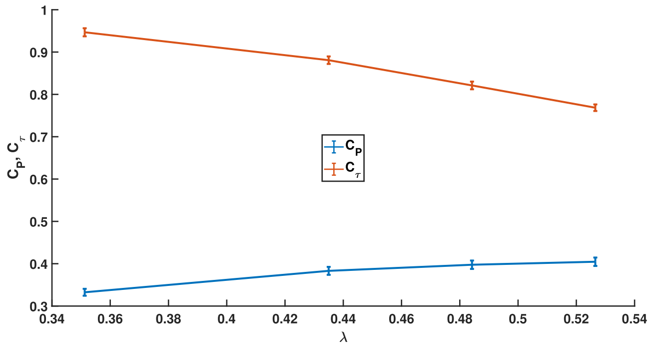

Fig. 13. C_P and C_τ against λ for Case E1-3.

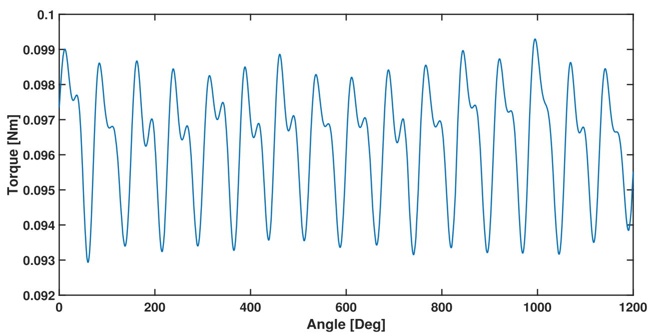

Fig. 14. Plot of filtered torque against angular position for Case E1-3. A low-pass filter at 250 Hz has been applied.

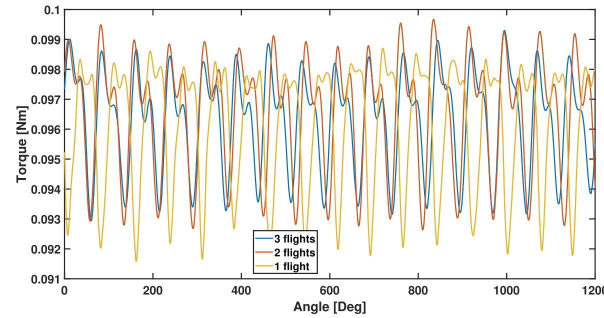

(a) Torque ripple for Cases E1-1, E1-2, and E1-3 over five revolutions.

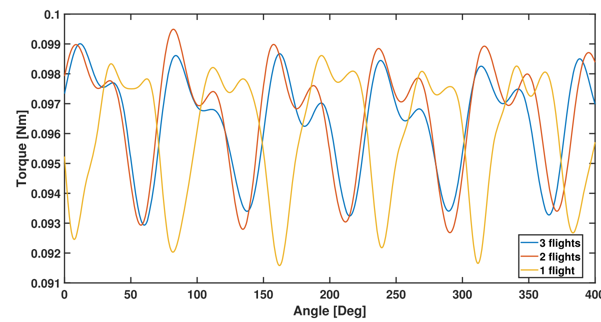

(b) Close-up view of torque ripple for cases E1-1, E1-2, and E1-3 over one revolution.

Fig. 15. Torque ripple for Cases E1-1, E1-2, and E1-3. All the torque measurements have been filtered at 250 Hz.

Table 4
TRP and TRF values for experimental cases. Values have been calculated over a duration of 60 seconds.

Case	TRP (%)	TRF (Nm)
E1-3	65.51	0.063
E1-2	170.07	0.164
E1-1	157.73	0.157
E2-3	21.71	0.017
E2-2	20.23	0.015
E2-1	76.56	0.045

The experimental results also showed a combination of a phase-dependent and a random variation in the torque output (torque ripple) as shown in Fig. 14. A Matlab low-pass Fourier transform filter function was used to filter out the effects of random fluctuations and noise in the raw data. A low-pass frequency (f_n) value of 250 Hz was used as it appeared to retain the vital signal information in the torque while removing the noise without distorting the signal significantly. It is also much greater than the turbine's rotational frequency, which has a range between 0.17 Hz and 0.83 Hz.

The torque ripple is defined as the cyclic fluctuation in the torque. It can be quantified as a percentage or as the arithmetic range of the torque as defined in Eqs. (12) and (13), respectively:

$$\text{TRP} = \frac{\tau_{\text{max}} - \tau_{\text{min}}}{\tau_{\text{mean}}} \times 100 \tag{12}$$

$$\text{TRF} = \tau_{\text{max}} - \tau_{\text{min}} \tag{13}$$

where TRP is the torque ripple percentage, TRF is the torque ripple function, and τ_{max} and τ_{min} are the maximum and minimum torque values, respectively, and τ_{mean} is the mean torque. Eqs. (12) and (13) are applied to the filtered data. For Case E1-3 shown in Fig. 14, the values of TRP and TRF are 65.51 % and 0.063 Nm, respectively, for a 60-second duration. Table 4 shows the values of TRP and TRF for the main cases detailed in this paper.

The ripples were observed to be a once-per-revolution occurrence and not once-per-flight; that is, irrespective of the number of flights (one, two or three), they were periodic with the turbine's revolution. Characterising and analysing the torque ripple and understanding its effects is important because it could potentially have consequences on power output and turbine performance and efficiency, as well as on the fatigue life of the drive train and generator. The nature, causes, and effects of this torque fluctuation/rippling are still poorly understood at this time and require further investigation. The only clue to its cause comes from Table 4, which shows the ripple differs significantly between the two configurations, suggesting that the different free-surface conditions are, at least, partly responsible.

Rippling has been reported in the literature on other types of turbines. Dellinger et al. (2016) attributed the torque ripple in ASGs to the fact that the first and last blades of the turbine are not subjected to the same fluid pressures, depending on the circumferential position of the screw and the filling of the buckets. They also recorded that the rippling reduced with an increase in the number of flights and the screw's length. They hence concluded that rippling depends on the filling of the buckets. For Darieus turbines, varying the pitch to accommodate higher solidity allowed power output to be maximised while reducing torque ripple (Winchester and Quayle, 2008).

Delafin et al. (2016) observed a reduction in torque ripple with an increase in the number of identical blades from two to three in vertical-axis wind turbines. This could be translated to an increase in N for the AST. Increasing N would effectively increase the solidity of the AST, which might result in a reduction in rippling. Increasing N is also likely to even out the hydrodynamic forces on the turbine, hence reducing torque ripple. As shown in Fig. 15 and Table 4, the ripple is more prominent in turbines with one and two flight(s) than those with three flights.

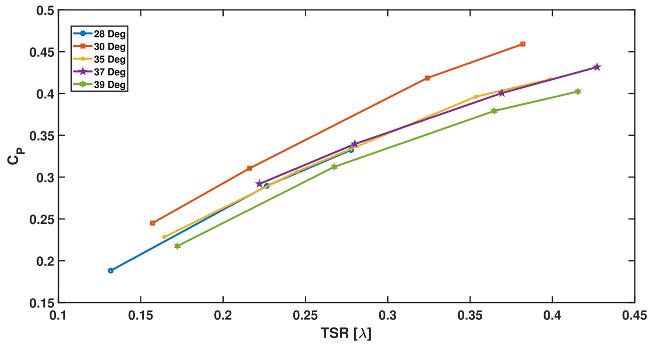

Fig. 16. C_P against λ for Case E2-v3.

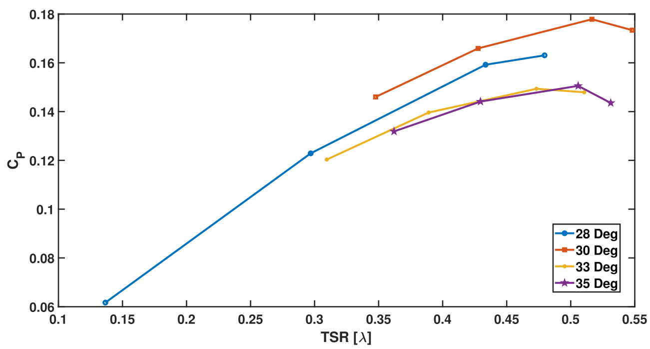

Fig. 17. C_P against λ for Case E2-v2.

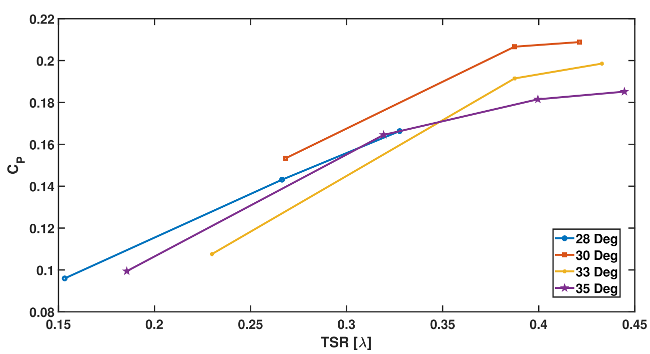

Fig. 18. C_P against λ for Case E2-v1.

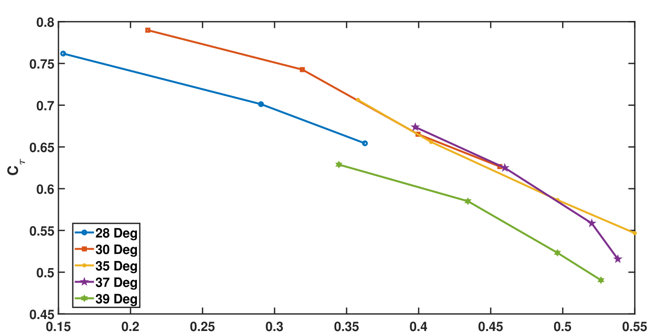

Fig. 19. C_τ against λ for Case E2-v3.

4.2. Torque and power results for the second configuration

Optimal performance was also achieved at 30° in the second configuration, with a maximum C_P of 0.34 at $\lambda = 0.54$ for three flights (Case E2-3). For the turbine with two flights (Case E2-2), maximum C_P of 0.17 was obtained at $\lambda = 0.54$ and 30°. The single-flight turbine (Case E2-1)

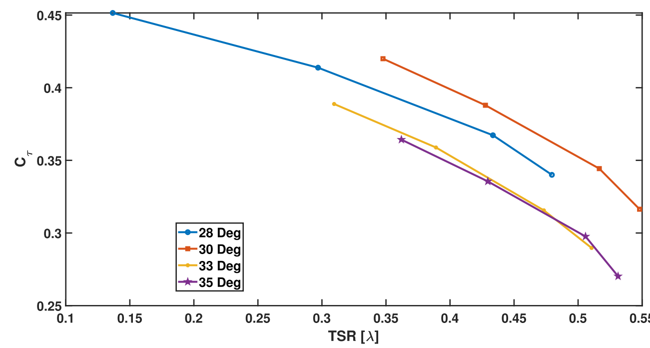

Fig. 20. C_τ against λ for Case E2-v2.

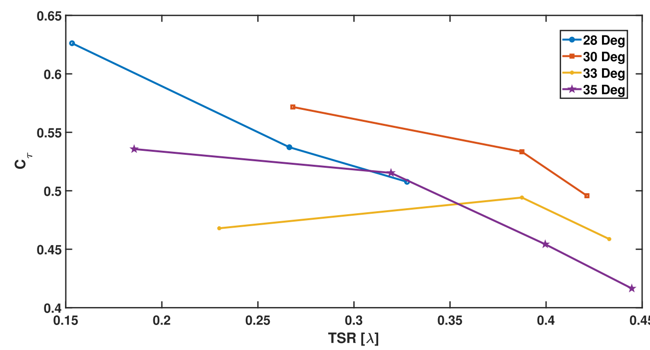

Fig. 21. C_τ against λ for Case E2-v1.

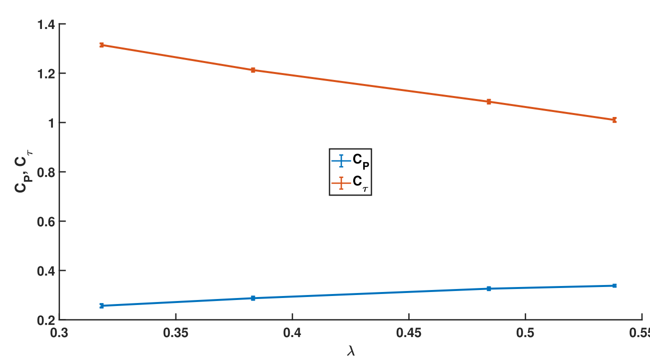

Fig. 22. C_P and C_τ against λ for Case E2-3.

achieved a maximum C_P of 0.21 at $\lambda = 0.42$ and 30°. Figs. 16–18 show the plots of C_P against λ for Cases E2-3, E2-2, and E2-1 respectively.

Figs. 19–21 show the corresponding plots of C_τ against λ. Fig. 22 shows the plots of both C_P and C_τ against λ with error bars included for Case E2-3. The figure shows that maximum C_τ is achieved at minimum C_P.

Table 5 summarises the experimental results for both configurations. Comparing the results for turbines with the same number of flights and at comparable tip speed ratios, it can be seen that the turbine performed generally better in the first configuration. The results also show that the turbine with three flights performed better than those with one and two flights. This significant difference in performance between the two configurations could be due to free surface effects, and it would be expected that for a turbine submerged far enough from the surface, the configuration would not matter to its performance.

Table 5
Summary of experimental results for both configurations.

Case	λ	C_P	C_τ
E1-3	0.53	0.40	0.76
	0.48	0.39	0.82
	0.43	0.38	0.88
	0.35	0.33	0.94
E1-2	0.52	0.41	0.79
	0.49	0.40	0.82
	0.42	0.37	0.88
	0.36	0.34	0.95
E1-1	0.30	0.23	0.76
	0.25	0.20	0.82
	0.15	0.13	0.88
E2-3	0.54	0.34	0.62
	0.48	0.32	0.66
	0.38	0.28	0.74
	0.31	0.25	0.78
E2-2	0.54	0.17	0.32
	0.51	0.18	0.34
	0.42	0.16	0.39
	0.35	0.15	0.42
E2-1	0.42	0.21	0.49
	0.38	0.20	0.53
	0.26	0.15	0.57

5. Summary and conclusion

This work discussed the experimental measurements of the AST's performance characteristics. The effects of different operating conditions were studied, including the effects of inclination angle β to determine optimal angle, the effects of the number of blades on performance, as well as quantifying the torque ripple in terms of TRP and TRF. Investigations of this kind have not been reported anywhere in the literature.

The results, as summarised in Table 5, showed that the turbine performed optimally for both configurations at $\beta = 30°$. A maximum C_P value of 0.4 was obtained for a 3-flight turbine in the first configuration at $\beta = 30°$, $\lambda = 0.53$, and $U_\infty = 0.45$ m/s. In the second configuration, maximum C_P was 0.34 at $\lambda = 0.54$ and $U_\infty = 0.45$ m/s. These experiments confirm the findings of Shahsavarifard et al. (2015) and Zhang et al. (2023) that the AST can achieve surprisingly high power outputs at low tip speed ratios and is thus a very appropriate candidate for tidal power generation.

There is a significant difference between the performance of the turbine in the two configurations. This suggests the importance of doing more detailed analyses of the flow field around the turbine to better understand how the two configurations differ. A CFD study could also shed light on the effects of the free surface on the difference in the performance of the two configurations. It can also show if the configuration remains unimportant in cases where surface effects are negligible.

The results also showed that the turbine with three flights generally performed better than those with one and two flight(s) in both configurations. Hence, it can be concluded that the turbine's performance improves with an increase in the number of flights. However, this work did not study the limit at which increasing number of flights leads to physical blockage in the turbine.

The torque measurements showed a combination of a phase-dependent and a random cyclic variation in the torque output, which reduced in magnitude with an increase in number of flights. The periodicity of the torque was found to occur once-per-revolution and not once-per-flight, irrespective of the number of flights. Additionally, the magnitude of this rippling decreased as the number of flights increased. The nature, causes, and effects of this torque fluctuation/rippling are still poorly understood at this time and require further investigation.

The large magnitude of the torque ripple implies a strongly periodic flow, which could make a steady CFD study unsuitable. In addition, the periodicity motivated a PIV study to investigate the periodicity of the flow around the turbine and to determine the applicability of a URANS numerical model in the CFD study. This work will be reported later.

The cause and effects of the rippling are still not understood, and it could have significant consequences for the turbine's efficiency and the lifespan of other components like the drive train and the generator. This makes future study of the torque ripple very important. The effects of blockage on the turbine's performance are also important and should be investigated.

6. Recommendations and future work

The opportunities for future work on the AST are numerous and, quite frankly, exciting. There is still so much unknown about the turbine, and any analysis which will lead to a better understanding of the flow mechanisms influencing the power extraction from the turbine would be very pertinent.

It is essential to study the influence of different geometric properties and design ratios (as discussed in Section 3) on turbine performance. Like with the ASG, these parameters and ratios could be vital for the turbine's operations and efficiencies. This can be done quickly and cheaply using CFD. CFD also allows different flow conditions, like the free stream velocity and blockage, to be varied. CFD can also be used to investigate the influence of surface effects on the performance of the two different configurations. It can show if the configuration remains unimportant in cases where surface effects are negligible.

The causes and effects of the rippling are still not understood, and it could have significant consequences for the turbine's efficiency and the lifespan of other components like the drive train and the generator.

CRediT authorship contribution statement

Temitope E. Phillips: Writing – review & editing, Writing – original draft, Methodology, Investigation, Conceptualization; **David H. Wood:** Writing – review & editing, Supervision, Conceptualization.

Declaration of competing interest

The authors declare that they have no known competing financial interests or personal relationships that could have appeared to influence the work reported in this paper.

Acknowledgements

The authors are grateful to the Schulich endowment to the University of Calgary for financial support. The authors would also like to thank Chris Morton, Ayman Ashry Mohammed, and Itoje Harrison for technical support with this project.

References

Alton, S.B., Howell, T.A., 2003. Displacement pumps. Encyclopedia of water science. Marcel Dekker. https://books.google.ca/books?id=0ApOPgAACAAJ 9780824742416

Consul, C.a., Willden, R.H.J., Ferrer, E., McCulloch, M.D., et al., 2009. Influence of solidity on the performance of a cross-flow turbine. In: Proceedings of the 8th European Wave and Tidal Energy Conference. EWTEC, Uppsala, Sweden, pp. 484–493. http://www.homepages.ed.ac.uk/shs/WaveEnergy/EWTEC2009/EWTEC2009(D)/papers/220.pdf.

Delafin, P.L., Nishino, T., Wang, L., Kolios, A., et al., 2016. Effect of the number of blades and solidity on the performance of a vertical axis wind turbine. J. Phys. Conf. Ser. 753 (2). https://doi.org/10.1088/1742-6596/753/2/022033

Dellinger, G., Garambois, P.A., Dufresne, M., Terfous, A., Vazquez, J., Ghenaim, A., 2016. Numerical and experimental study of an Archimedean screw generator. IOP Conference Series: Earth and Environmental Science vol. 49 (10). https://doi.org/10.1088/1755-1315/49/10/102002

Eltayesh, A., Hanna, M.B., Castellani, F., Huzayyin, A.S., El-Batsh, H.M., Burlando, M., Becchetti, M., 2019. Effect of wind tunnel blockage on the performance of a horizontal axis wind turbine with different blade number. Energies 12 (10), 1–15. https://doi.org/10.3390/en12101988

Jeong, H., Lee, S., Kwon, S.D., 2018. Blockage corrections for wind tunnel tests conducted on a Darrieus wind turbine. J. Wind Eng. Ind. Aerodyn. 179 (June), 229–239. https://doi.org/10.1016/j.jweia.2018.06.002

Kinsey, T., Dumas, G., 2017. Impact of channel blockage on the performance of axial and cross-flow hydrokinetic turbines. Renew. Energy 103, 239–254. https://doi.org/10.1016/j.renene.2016.11.021

Kolekar, N., Banerjee, A., 2015. Performance characterization and placement of a marine hydrokinetic turbine in a tidal channel under boundary proximity and blockage effects. Appl. Energy 148, 121–133. https://doi.org/10.1016/j.apenergy.2015.03.052

Kozyn, A., Ash, S., Lubitz, David, W., 2015. Assessment of Archimedes screw power generation potential in Ontario. In: Climate Change Technology Conference. IEEE, Canada, Montréal, QC, pp. 123–128. https://doi.org/10.1007/978-1-4614-7495-1_23

Lashofer, A., Hawle, W., Kampel, I., Kaltenberger, F., Pelikan, B., et al., 2012. State of technology and design guidelines for the Archimedes screw turbine. In: Hydro 2012 - Innovative Approaches to Global Challenges. The international Journal on Hydropower & Dams, Bilbao, Spain, pp. 1–8.

Lyons, M., Lubitz, W.D., 2013. Archimedes screws for microhydro power generation. In: ASME 2013 7th Int. Conf. on Energy Sustainability Collocated with the ASME 2013 Heat Transfer Summer Conf. and the ASME 2013 11th Int. Conf. on Fuel Cell Science, Engineering and Technology, ES 2013. ASME, Minneapolis. https://doi.org/10.1115/ES2013-18067

Moffat, R.J., 1982. Contributions to the theory of single-sample uncertainty analysis. J. Fluids Eng. Trans. ASME 104 (2), 250–258. https://doi.org/10.1115/1.3241818

Müller, G., Senior, J., 2009. Simplified theory of archimedean screws. J. Hydraul. Res. 47 (5), 666–669. https://doi.org/10.3826/jhr.2009.3475

Nagel, G., 1968. Archimedean Screw Pump Handbook. RITZ Pumpenfabrik OHG, Schwabisch Gmund. https://www.frenchriverland.com/archimedian_screw_pump_handbook_gerhard_nagel.htm.

Omega Engineering, 2000. Rotating sensors: shaft-to-shaft configuration. https://assets.omega.com/pdf/test-and-measurement-equipment/load-and-force/torque-sensors/TQ513.pdf?_hstc=257583444.0222e5d2723762e6af702b35c947c462.1700674925059.1700674925059.1700674925059.1&_hssc=257583444.4.1700674925060&_hsfp=4253508547.

Phillips, T.E., 2024. Experimental and Computational Study of the Archimedes Screw Turbine. Ph.D. thesis. University of Calgary. https://prism.ucalgary.ca/bitstreams/8b5b284c-1e68-487a-bf3e-021af02806b1/download.

Rohmer, J., Knittel, D., Sturtzer, G., Flieller, D., Renaud, J., 2016. Modeling and experimental results of an Archimedes screw turbine. Renew. Energy 94, 136–146. https://doi.org/10.1016/j.renene.2016.03.044

Rolling Hills Research Corporation, 2003. Research water tunnels: specifications.

Rorres, C., 2000. The turn of the screw: optimal design of an Archimedes screw. J. Hydraul. Eng. 126 (1), 72–80. https://doi.org/10.1061/(ASCE)0733-9429(2000)126:1(72)

Ross, H., Polagye, B., 2020. An experimental assessment of analytical blockage corrections for turbines. Renew. Energy 152, 1328–1341. https://doi.org/10.1016/j.renene.2020.01.135

Shahsavarifard, M., Birjandi, A.H., Bibeau, E.L., Sinclaire, R., et al., 2015. Performance characteristics of the energy cat 3EC42 hydrokinetic turbine. MTS/IEEE OCEANS 2015 - Genova: Discovering Sustainable Ocean Energy for a New World , 1–4. https://doi.org/10.1109/OCEANS-Genova.2015.7271420

Shahverdi, K., Loni, R., Maestre, J.M., Najafi, G., 2021. CFD numerical simulation of Archimedes screw turbine with power output analysis. Ocean Eng. 231, 108718. https://doi.org/10.1016/j.oceaneng.2021.108718

Shimomura, M., Takano, M., 2013. Modeling and performance analysis of Archimedes screw hydro turbine using moving particle semi-implicit method. J. Comput. Sci. Technol. 7 (2), 338–353. https://doi.org/10.1299/jcst.7.338

Simmons, S., Lubitz, W., 2017. Archimedes screw generators for sustainable energy development. IHTC 2017 - IEEE Canada International Humanitarian Technology Conference 2017 , 144–148. https://doi.org/10.1109/IHTC.2017.8058176

Taylor, J.R., Thompson, W., 1998. An introduction to error analysis: the study of uncertainties in physical measurements. https://doi.org/10.1063/1.882103

Thakur, R., Kashyap, T., Kumar, R., Saini, R.K., Lee, D., Kumar, S., Singh, T., 2024. Potential of the Archimedes screw to generate sustainable green energy for mini, micro, and pico hydro turbine power stations: an extensive analysis. Energy Strategy Rev. 55, 101514. https://doi.org/10.1016/j.esr.2024.101514

Waters, S., 2015. Analysing the Performance of the Archimedes Screw Turbine within Tidal Range Technologies. Ph.D. thesis. Lancaster University.

Waters, S., Aggidis, G.A., 2015. Over 2000 years in review: revival of the Archimedes screw from pump to turbine. Renew. Sustain. Energy Rev. 51, 497–505. https://doi.org/10.1016/j.rser.2015.06.028

Williamson, S.J., Stark, B.H., Booker, J.D., 2011. Low head pico hydro turbine selection using a multi-criteria analysis. In: Moshfegh, P.B. (Ed.), World Renewable Energy Congress. Linköping University Electronic Press, Linköping, Sweden, pp. 1377–1385. http://www.ep.liu.se/ecp_home/index.en.aspx?issue=057.

Winchester, J.D., Quayle, S.D., 2008. Torque ripple and power optimisation of variable pitch vertical axis tidal turbines. Eng. Phys. Sci. Res. Counc. , 80210.

Zhang, D., Guo, P., Hu, Q., Li, J., 2022. Parametric study and multi-objective optimization of a ductless Archimedes screw hydrokinetic turbine: experimental and numerical investigation. Energy Convers. Manage. 273 (September), 116423. https://doi.org/10.1016/j.enconman.2022.116423

Zhang, D., Guo, P., Wang, Y., Hu, Q., Li, J., 2023. Performance analysis of a ductless Archimedes screw turbine array for deep-sea power supply. Ocean Eng. 288 (P2), 116113. https://doi.org/10.1016/j.oceaneng.2023.116113

Zitti, G., Fattore, F., Brunori, A., Brunori, B., Brocchini, M., 2020. Efficiency evaluation of a ductless Archimedes turbine: laboratory experiments and numerical simulations. Renew. Energy 146, 867–879. https://doi.org/10.1016/j.renene.2019.06.174